Journal of Materials Chemistry A

ROYAL SOCIETY OF CHEMISTRY

COMMUNICATION

View Article Online
View Journal | View Issue

Cite this: J. Mater. Chem. A, 2021, 9, 11553

Received 6th October 2020
Accepted 7th April 2021

DOI: 10.1039/d0ta09738a

rsc.li/materials-a

Computational design of a switchable heterostructure electrocatalyst based on a two-dimensional ferroelectric In_2Se_3 material for the hydrogen evolution reaction†

Han Seul Kim *[ab]

A theoretical design for an ON–OFF switchable HER catalyst using the two-dimensional ferroelectric (2D-FE) III_2VI_3 compound In_2Se_3 is reported in this paper. With vertical stacking of the basal plane of In_2Se_3 on top of the transition metal cobalt, a set of *ab initio* calculations reveals that the reversible polarization switching of In_2Se_3 can turn the HER activity of the heterostructure ON and OFF. The principle of HER activation/deactivation of the heterostructure is discussed in terms of the electronic structures, and the polarization-dependent modulation of electronic energy and charge transfer between In_2Se_3 and the transition metal are identified as the key factors. The distinct electron transfer mechanisms for the structures based on mono- and bilayers of In_2Se_3 are identified in terms of the different electronic connections between Co and In_2Se_3, and the structures are labelled as "direct" and "indirect" catalysts, respectively. This work provides insight into a possible pathway for designing dynamically controlled electrocatalysts based on 2D materials without introducing any chemical disorder.

Introduction

Recent years have witnessed an exploding interest and fast development in two-dimensional ferroelectric materials (2D-FEs).[1,2] 2D-FEs have reversible polarization that can be manipulated by external stimuli, even within their extremely thin atomic structures. Among many such materials, a class of two-dimensional III_2VI_3 compounds,[3,4] which is one subgroup of the two-dimensional transition metal chalcogenides (2D-TMCs), is of particular interest. Various ferroelectric two-dimensional III_2VI_3 compounds with quintuple-layer (five-atom-thick) structures have recently been proposed through simulations, of which In_2Se_3 has been the most actively studied example of 2D-FE III_2VI_3 for the last few years in both theoretical and experimental works. After the theoretical estimations on the presence of in-plane and out-of-plane ferroelectricity in ground-state α-phase In_2Se_3,[5,6] such ferroelectric behaviour was also observed experimentally.[7–9] Owing to the interesting reversible polarization switching that can be enabled by applying an electric field, various applications such as ferroelectric memory[10,11] and gas sensing[12] have been suggested. To expedite the practical applications of In_2Se_3, advances such as large-area and ultrafast synthesis have also been pursued.[13]

One compelling yet barely explored application of 2D-FE In_2Se_3 is as an electrocatalyst for which the simplest version is the hydrogen evolution reaction (HER) catalyst. Notably, recent computational studies have brilliantly demonstrated that In_2Se_3 shows reversible gas capture/release based on its polarization switching[12] and exhibits adequate built-in potential for photocatalyst applications.[14,15] This implies that In_2Se_3 can be utilized as an on/off reversible (photo-)catalyst after further manipulation of the molecular binding energies. Then, design of 2D-FE-based electrocatalyst structures with enhanced molecular adsorption and appropriate reaction energies by explicitly assessing the catalytic reaction should be the next step. In line with active researches on switchable catalysts using bulk ferroelectric materials,[16,17] the investigation of possible approaches for the utilisation of 2D-FE In_2Se_3 as a switchable electrocatalyst is a highly promising research direction. In fact, stimuli-controlled and on–off switchable electrocatalysis for on-demand hydrogen production is particularly important for efficient hydrogen generation in portable devices.[18–21] Furthermore, creative applications using on–off switchable electrocatalysts such as multiple stimuli-switchable electrocatalysis and logic gates have also been demonstrated.[22]

Meanwhile, the semiconducting nature and weak molecular adsorption of the basal plane have been pointed out as the main obstacles in the use of 2D-TMCs as electrocatalysts. It is a well-known design rule that the adsorption energy of catalytic

[a]Centre for Supercomputing Applications, National Institute of Supercomputing and Networking, Korea Institute of Science and Technology Information (KISTI), Daejeon 34141, Republic of Korea. E-mail: hanseulkim0@kisti.re.kr

[b]Department of Data & High Performance Computing Science, University of Science & Technology (UST), Daejeon 34113, Republic of Korea

† Electronic supplementary information (ESI) available. See DOI: 10.1039/d0ta09738a

intermediates on the catalytic surface should be moderate (not too high or too low).[23,24] Therefore, boosting the molecular adsorption on the 2D-TMC surface is critical for effective utilisation of the large surface area and capability of atomic/electronic tuning[25–27] of 2D-TMCs for electrocatalyst applications. Researchers have focused on modifying the atomic/electronic structures of 2D-TMCs to enhance molecular adsorption by exposing edges and introducing atomic defects and metastable metallic phases.[28–34] Constructing hetero-interfaces of 2D materials with metal substrates can be a more general approach for the systematic design of 2D-based HER catalysts without introducing chemical treatments.[27,35]

This work presents the computational design of an ON–OFF switchable HER catalyst with systematic tuning of the hydrogen adsorption energy by constructing vertical heterostructures based on 2D-FE III_2VI_3 In_2Se_3 and the transition metal cobalt. Cobalt is chosen because it is a non-precious transition metal with ferromagnetic properties. Brief results with reactive and inert diamagnetic metals, Cu and Au, will also be provided for comparison. Adopting a set of density functional theory (DFT) calculations, the effect of the ferroelectric polarity of In_2Se_3 on hydrogen adsorption will be first discussed based on the electronic structures. Then, the construction of Co + In_2Se_3 vertical heterostructures will be suggested as a powerful approach to amplify the effect of polarity to modulate HER efficiency. In these heterostructures, the HER activity can be turned on and off by ferroelectrically switching the polarity of In_2Se_3. The principles behind the relationship between the polarity and HER activity will be provided in view of electronic hybridizations between Co and In_2Se_3 and manipulation of the electronic states of In_2Se_3. The distinct origins of the HER activities for Co + In_2Se_3 complexes with mono- and bilayer In_2Se_3 will also be thoroughly discussed in terms of the electron transfer mechanisms. By devising a 2D-FE In_2Se_3 heterostructure for a switchable HER catalyst, this work will pave the way for the future design of dynamically controlled electrocatalysts using III_2VI_3 and other 2D ferroelectric materials.

Computational methods

Model preparation

The ground state of the ferroelectric α-In2Se$_3$ has two degenerate phases, namely ferroelectric zincblende (FE-ZB′) and wurtzite (FE-WZ′) (ESI Fig. S1†). Among the two phases, FE-ZB′ was chosen to study the HER activities as in a previous report.[6] According to the ferroelectric polarization (**P**) direction of In_2Se_3, which is defined by the location of the central Se atom (Se_c), upward (**U**) and downward (**D**) polarizations models were defined (Fig. 1a). The 3 × 3 supercells of FE-ZB′ were prepared to adsorb H atoms to ensure that the distance between the H atoms in the neighbouring cells was larger than 12 Å. Thus, the effect of the adsorption density was ignored in this study.

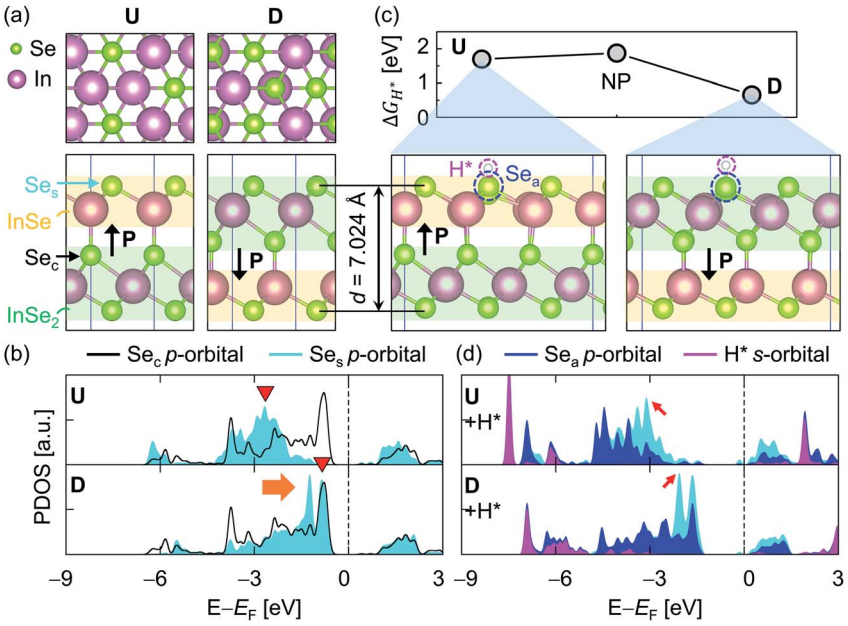

Fig. 1 (a) The atomic structures of monolayer FE-ZB′ In_2Se_3 with upward (**U**) and downward (**D**) out-of-plane polarizations. Top views (top) and side views (bottom) visualize how the positional shift of the Se_c results in unique polarization switching. Se_s indicates the surface Se atoms that will become active sites when adsorbing H*. The yellow and green shaded areas represent the InSe and $InSe_2$, which are the substructures of In_2Se_3, respectively. d = 7.024 Å and **P** indicate the separation between the two In_2Se_3 layers and the polarization direction, respectively. (b) The projected density of states (PDOS) for **U** and **D**. The black lines and cyan-coloured areas indicate the p-orbital states of Se_c and Se_s, respectively. The orange arrow highlights the remarkable upshift of Se_s states due to the position change of Se_c. The red downward triangles indicate the position of the p-band peak for Se_s ($\varepsilon_{p\text{-}peak}$). (c) The calculated free energies of hydrogen adsorption (ΔG_{H^*}) for different ferroelectric polarizations: **U**, **D**, and a nonpolarized phase (**NP**; face-centred cubic In_2Se_3, as shown in Fig. S1†). Se_a indicates an active Se_s atom where the H* is attached. (d) PDOS for the hydrogen-adsorbed **U** and **D**. The blue- and magenta-coloured areas are the p-orbital states of Se_a and s-orbital state of H*, respectively. The red arrows indicate the electronic states of Se_s that contribute to bond formations with H*.

Meanwhile, a four-layer hexagonal close-packed (HCP) Co metal slab along the basal (0001) plane was prepared. Then, a 5 × 5 supercell Co was generated and scaled to the 3 × 3 supercell of In_2Se_3 FE-ZB′ to construct a vertical heterostructure. The lattice misfit between 5 × 5 Co and 3 × 3 In_2Se_3 was only 1%. The details are provided in Fig. S2.†

Electronic structure calculations

All of the DFT simulations were performed to calculate the total energies and vibrational frequencies within the grid-based projector-augmented wave method as implemented in the GPAW package.[36] The revised Perdew–Burke–Ernzerhof (RPBE) functional was adopted as the exchange–correlation functional,[37] and the wavefunctions were expanded on a real space grid with a grid spacing of 0.14 Å. Fermi smearing of 0.1 eV was used, and the calculations were performed on the periodically repeated unit cells and 3 × 3 supercells of In_2Se_3 with 8 × 8 × 1 and 2 × 2 × 1 Monkhorst–Pack Brillouin zone sampling, respectively. Spin polarization was considered for all calculations. As an eigensolver, the residual minimization method–direct inversion in iterative subspace (RMM–DIIS) was utilized.[38,39] All of the structures were optimized using the conjugate-gradient method until the maximum force on any unconstrained atom was less than 0.05 eV $Å^{-1}$. A vacuum space of 18 Å was adopted after a series of test calculations (Fig. S3†) to avoid artificial interactions between periodic images, and the dipole correction was applied to describe the properties of the slab accurately. The effects of the calculation parameters such as the self-consistent-field convergence criterion and force-convergence criterion were thoroughly tested, and the parameters that give cost-effective yet accurate estimations on ΔG_{H^*} were adopted for the data generation. The details are provided in Table S1.†

Free energy calculations

ΔG_{H^*} is a reliable descriptor for HER activity under acidic conditions.[23,24] The free energies of the atomic hydrogen adsorptions were calculated to evaluate the HER activity as:

$$\Delta G_{H^*} = \Delta E_{H^*} + \Delta E_{ZPE} - T\Delta S_{H^*} \quad (1)$$

where ΔE_{H^*} is the hydrogen adsorption energy, ΔE_{ZPE} is the difference in the zero-point energy (E_{ZPE}) between the adsorbed (H*) and the gas-phase hydrogens (H_2), T is the temperature (298.15 K in this work), and ΔS_{H^*} is the entropy change due to adsorption. It is well known that highly efficient HER catalysts are characterized by $|\Delta G_{H^*}| \cong 0 < 0.20$ eV.[40] The hydrogen adsorption energies were computed as

$$\Delta E_{H^*} = E_{sub+H} - (E_{sub} + 1/2E_{H_2}), \quad (2)$$

where E_{sub+H}, E_{sub}, and E_{H_2} indicate the total energies of the hydrogen-adsorbed substrate, the bare substrate, and the isolated hydrogen gas in a vacuum, respectively.

The free energy corrections (ΔE_{ZPE} and $T\Delta S_{H^*}$) were defined as:

$$\Delta E_{ZPE} = E_{ZPE,1L+H^*} - (E_{ZPE,1L} + 0.5 \times E_{ZPE,H_2}), \quad (3)$$

$$\Delta S_{H^*} = S_{1L+H^*} - (S_{1L} + 0.5 \times S_{H_2}), \quad (4)$$

where 1L and 1L + H* indicate the monolayer In_2Se_3 and hydrogen-adsorbed 1L, respectively. The values of ΔE_{ZPE} and $T\Delta S_{H^*}$ were explicitly computed on the basis of statistical thermodynamics from the vibrational frequencies by adopting the small displacement method based on the harmonic approximation as implemented in the ASE package[41] where GPAW is plugged in as an electronic structure calculator.[42,43] The displacement amplitude of 0.015 Å was adopted.

The E_{ZPE} was computed by summing the vibrational frequencies over all of the normal modes ν_i,

$$E_{ZPE} = 1/2\sum_{i}^{k} \hbar\nu_i \quad (5)$$

where $\hbar$ is Planck's constant divided by 2π, i is the normal mode index, and k is the number of vibrational modes. The entropy, S, is given by[44]

$$S(T) = \sum_{i=1}^{3N}\left(-R\ \ln\left(1 - e^{-h\nu_i/k_BT}\right) + \frac{N_A h\nu_i}{T}\frac{e^{-h\nu_i/k_BT}}{1 - e^{-h\nu_i/k_BT}}\right), \quad (6)$$

where R is the universal gas constant, k_B is Boltzmann's constant, h is Planck's constant, N_A is Avogadro's number, and N is the number of adsorbed atoms. Eqn (5) and (6) indicate that E_{ZPE} and $S(T)$ are dominated by high- and low-frequency modes, respectively. For gas-phase hydrogens, the standard state entropies are considered in most cases.[45] On the other hand, the entropy of the surface species is neglected in most studies since adsorbed hydrogen vibrates at high frequency.

However, it is important to explicitly calculate all of the relevant terms because the catalytic activities of In_2Se_3 have not been studied previously. Therefore, all of the stationary modes of monolayer In_2Se_3 (1L) with and without adsorbed hydrogen were examined in this study using eqn (3)–(6). The vibrational density of states (VDOS) for 1L, 1L + H*, and gaseous H_2 was obtained from the separate calculations without fixing any of the atoms. The details are summarized in Fig. S4 and Table S2† by showing the VDOS of 1L with/without adsorbed hydrogen and gas-phase hydrogens, and the energy correction is obtained as $\Delta E_{ZPE} - T\Delta S_{H^*} = -0.0091 + 0.0359 = 0.0268$ eV. Interestingly, the infinitesimal ΔE_{ZPE} indicates that the hydrogen adsorbed on selenium (4p) is relatively stable compared to that on carbon (2p, 0.17 eV).[45]

Results and discussion

HER activities of monolayer In_2Se_3: an indication of ferroelectricity-enabled HER control

Fig. 1a shows the atomic structures of the 1L FE-ZB′ α-In_2Se_3 with **U** and **D** polarization states. The **U**/**D** states of the polarization are achieved simply by shifting the vertical position of the Se_c atom down/up by external stimuli such as the electric field. The Se atom on the top surface is marked as Se_s and its position remains unchanged during polarization switching.

Based on its quintuple-layer structure, the structure of In_2Se_3 can be further divided into two substructures, InSe and $InSe_2$, as indicated in Fig. 1a by the yellow and green shaded areas, respectively. Accordingly, switching from **U** and **D** modifies the configuration of In_2Se_3 from "$InSe_2$ (bottom) + InSe (top)" to "InSe (bottom) + $InSe_2$ (top)". A step-by-step procedure of the ferroelectric switching of FE-ZB′ In_2Se_3 and the corresponding energy barrier diagram are provided in ESI Fig. S5.†

Polarization switching significantly modifies the projected density of states (PDOS) of FE-ZB′, as depicted in Fig. 1b. Unlike for transition metal catalysts, the p-orbital states of the active surface play the key role in HER on 2D-TMC.[46–48] In particular, the proximity of the valence band (VB) contribution of the Se_s p-states (the filled p-orbitals) to the Fermi energy (E_F) is of central importance. More specifically, the energetic location of the p_z-state is worth considering because the electrons should be transferred from the In_2Se_3 surface to adsorbed hydrogen by forming the bonding between Se $4p_z$ and H 1s to activate HER as shown in Fig. S6 and S7.†[49] To quantify the details for the location of the p_z-states of Se_s, the $4p_z$-band centre (ε_{pz}-centre) can be introduced. ε_{pz}-centre represents the energetic location of the centre of $4p_z$-states, analogous to the well-known d-centre:[49–51]

$$\varepsilon_{p_z\text{-centre}} = \frac{\int_{-\infty}^{+\infty} E D_{p_z}(E)\mathrm{d}E}{\int_{-\infty}^{+\infty} D_{p_z}(E)\mathrm{d}E}, \quad (7)$$

where E and $D_{pz}(E)$ are the electronic energy and PDOS for the $4p_z$-orbital states of Se_s, respectively. The $\varepsilon_{p\text{-centre}}$ can also be defined in the same manner but by adopting the PDOS of the averaged 4p-orbital states of Se_s, $D_{pz}(E)$, in eqn (7) and the *p*-band peak ($\varepsilon_{p\text{-peak}}$) can be defined as the energy of the highest PDOS peak for *p*-Se_s below E_F. The trend of changes in values depending on the model is the same in all three of $\varepsilon_{pz\text{-centra}}$, $\varepsilon_{p\text{-centre}}$, and $\varepsilon_{p\text{-peak}}$. By definition, $\varepsilon_{pz\text{-centre}}/\varepsilon_{p\text{-centre}}$ identifies the energetic location of the filled p_z/p-orbital of the active surface. The values are given as negative numbers by setting $E_F = 0.0$ eV. The closer the values are to zero, the closer the energies of the states are to E_F. Thus, $\varepsilon_{pz\text{-centre}}$ will be a useful indicator for assessing ΔG_{H^*}. However, PDOS plots throughout this paper will be provided based on the averaged 4p-band states of the Se atoms, which include information about all the p_x, p_y, and p_z orbitals.

While the PDOS of Se_c remains unchanged, the $\varepsilon_{pz\text{-centre}}/\varepsilon_{p\text{-centre}}$ of Se_s is −2.86/−3.26 eV in **U** and −1.67/−2.03 eV in **D**, which is an indication of a significant peak shift of ∼1.60 eV during polarization switching. This means that the electronic states of Se_c hybridize/dehybridize with those of Se_s by forming $InSe_2$/InSe, depending on the position in **D**/**U**. Therefore, the atomic movement of Se_c in **D**/**U** effectively turns ON/OFF the near-E_F contribution of the filled Se_s p-states, while the electronic state of Se_c itself is unchanged. Note that the spin-polarization was considered in the calculations and only the *α*-spin component is presented in the PDOS plot after checking that there is no significant difference between the PDOS of the two spin components.

It should be highlighted that the built-in potential within In_2Se_3 takes a key role in the polarization-dependent switching of the $\varepsilon_{pz\text{-centre}}$. The intrinsic dipole directs from the $InSe_2$ to InSe substructure within the In_2Se_3, as can be seen from the bond dipoles (BDs) between the two substructures (Fig. S8†). The H* adsorption on In_2Se_3 induces a negative bond dipole, which reduces/amplifies the dipole moment of 1L(**D**)/1L(**U**) (Fig. S8†). Correspondingly, the location of $\varepsilon_{pz\text{-centre}}$ (and $\varepsilon_{p\text{-centre}}$) with respect to E_F is manipulated due to the polarization-dependent built-in potential (Fig. S9†). This means that the polarization-dependent local bonding environment of In_2Se_3 plays an essential role in modulating hydrogen adsorption while the built-in electric field plays a supporting role, as previously reported for a Janus MoSSe monolayer.[52]

Owing to the manipulated locations of the filled Se_s p-states, the simple reversal of the polarization direction from **U** to **D** remarkably reduces the free energies of hydrogen adsorption (ΔG_{H^*}) by more than 1.0 eV, from 1.74 eV to 0.71 eV (Fig. 1c). The ΔG_{H^*} for models **U** and **D** are obtained using eqn (1) by attaching hydrogen (H*) onto one of the Se_s atoms (an active Se; Se_a) in the 3 × 3 supercells of monolayer In_2Se_3 (ESI Fig. S10†). The H*–Se_a bond formation on **U** at the InSe substructure is highly endothermic and accompanied by noticeable surface distortions. Correspondingly, the entire downward shift of the filled p-state (indicated by the red arrows) is observed upon H adsorption (Fig. 1d). On the other hand, **D** undergoes only a negligible surface distortion upon H adsorption on the $InSe_2$ substructure, and only the local valence band maximum − 1 (VBM-1) peak of p-Se_s at E_F − 2.49 eV shifts downward in Se_a (denoted by a red arrow in Fig. 1d) upon Se–H bond formation.

Note that, unfortunately, ΔG_{H^*} is still too large in both the **U** and **D** cases for an isolated In_2Se_3 to become a suitable HER catalyst. Similar to other 2D-TMCs,[53,54] the hydrogen adsorption will be too weak on isolated In_2Se_3. More thorough investigations into the relationship between the ferroelectric polarization and ΔG_{H^*} is provided in ESI Fig. S11.† **D** favours HER better than **U**, while HER is not activated in all cases even with the bilayer In_2Se_3 (2L), as will be shown in the later part of this paper.

The "direct" switchable catalyst: a case with Co + a monolayer of In_2Se_3

To exploit the polarization-dependent modulation of ΔG_{H^*} for turning the HER activity on and off, H* adsorption on In_2Se_3 should be amplified. Constructing vertical heterostructures with metal substrates is one effective approach in this regard, as in the cases of other 2D materials.[27,35] As a metal substrate, the transition metal Co is employed in this work. The ferromagnetism of Co can be pointed out as a key factor in 'turning on' the HER of In_2Se_3 upon heterostructuring, by breaking the spin degeneracy of In_2Se_3 so that its electronic states move toward E_F (Fig. S12†). By contrast, HER is not activated when adopting diamagnetic metals such as Au and Cu (Fig. S13†). Details of the metal species-dependency can be provided in the following work, and this study will focus on the design of an ON–OFF switchable HER catalyst using a Co metal slab.

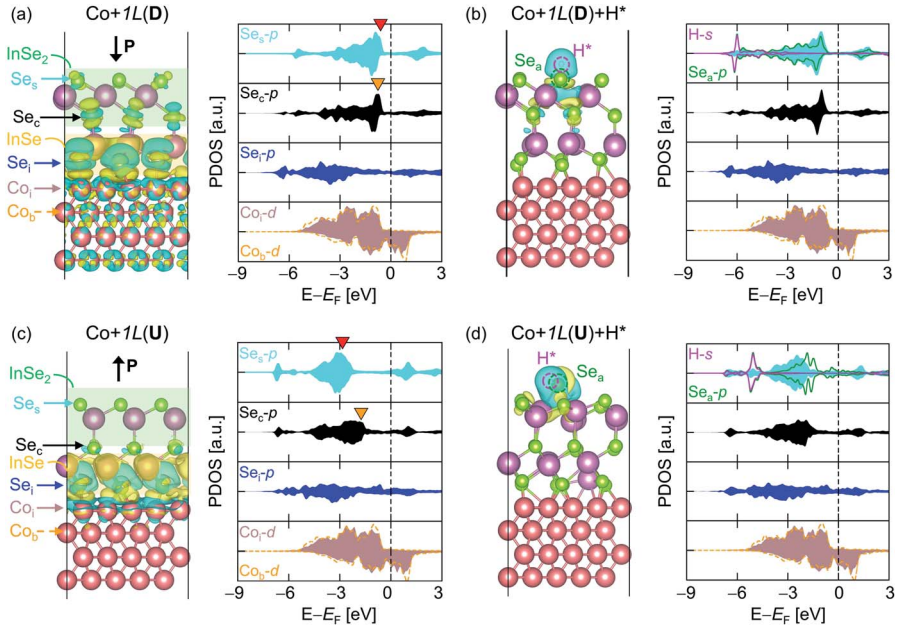

Fig. 2 Charge density differences and PDOS plots for (a) Co + 1L(**D**), (b) Co + 1L(**D**) + H*, (c) Co + 1L(**U**), and (d) Co + 1L(**U**) + H*. The green and yellow shaded areas indicate $InSe_2$ and InSe substructures within In_2Se_3, respectively. The isovalue is 0.001 e Å^{-3}, while the yellow and cyan colours represent positive and negative values, respectively. The cyan, black, and blue areas in the PDOS indicate the p-orbital states of Se_s, Se_c, and Se_i, respectively. The brown shaded areas and orange dashed lines indicate the d-orbital states of Co_i and Co_b, respectively. The red and orange downward triangles indicate the position of the p-band peaks for Se_s ($\varepsilon_{p\text{-peak}}$) and Se_c, respectively.

By stacking monolayer In_2Se_3 on top of Co (Co + 1L), the strong effect of Co converts the electronic structure of 1L to be more favourable for H* adsorption. Fig. 2a and b respectively show the charge density differences (CDDs) of Co + 1L(**D**) and Co + 1L(**D**) + H*. The CDD of 1L vertically stacked on a Co metal slab is defined as:

$$\Delta\rho_{Co\,+\,1L} = \rho_{Co\,+\,1L} - (\rho_{Co} + \rho_{1L}) \quad (8)$$

where $\rho_{Co\,+\,1L}$, ρ_{Co}, and ρ_{1L} indicate the spatial charge densities of the Co + 1L composite, Co slab, and 1L, respectively. Similarly, the CDD due to an H* adsorbed on Co + 1L is:

$$\Delta\rho_{[Co\,+\,1L]\,+\,H^*} = \rho_{[Co\,+\,1L]\,+\,H^*} - (\rho_{Co\,+1L} + \rho_H), \quad (9)$$

where $\rho_{[Co\,+\,1L]\,+\,H^*}$ and ρ_H indicate the spatial charge densities of the hydrogen-adsorbed Co + 1L and an isolated hydrogen atom, respectively. The Co–InSe interface in Co + 1L(**D**) undergoes a noticeable charge transfer and $\Delta\rho_{Co\,+\,1L(\mathbf{D})}$ is easily delocalized through the Se_c atom in the middle. Consequently, the meaningful charge density difference is observed even at the top $InSe_2$ surface. This excessive charge (coloured in yellow) on top of the active surface will assist hydrogen adsorption as a 'glue' at the active surface. On the other hand, the effect of Co on the surface charge density of Se_s is negligible in the case of Co + 1L(**U**) (Fig. 2c). $\Delta\rho_{Co\,+\,1L(\mathbf{U})}$ is localized at the Co–$InSe_2$ interface so that the hydrogen adsorption on Co + 1L(**U**) benefits less from the charge transfer between Co and In_2Se_3 (Fig. 2d).

The corresponding PDOS plots shown on the right hand sides of Fig. 2a–d more closely reveal the origin of the catalytic activities. Since the ferromagnetic properties of Co induce the spin splitting of In_2Se_3 (Fig. S12†), α and β spins are shown in the positive and negative DOS regions, respectively. The Se atoms at the Co–In_2Se_3 interface (Se_i) strongly hybridize with the interface Co atoms (Co_i), both for Co + 1L(**U**) and Co + 1L(**D**) (Fig. 2a and c). Furthermore, Se_c and Se_s become slightly metallic owing to having a finite value in the bandgap region of In_2Se_3 (Fig. S12 and S14†). Having a synergistic effect with strain caused by chemical bonding, this promotes charge transfer from the electron reservoir Co to the In_2Se_3 active surface. This is consistent with the recent studies demonstrating that the synergistic effects of local bonding and charge transfer related to surface states can tune the adsorption properties of the surfaces.[55,56] Such adjustments of the surface adsorption characteristics can even control the growth modes of the thin film and the stability of the catalyst.

Meanwhile, the intrinsic built-in potential of In_2Se_3 (Fig. S15†) polarization-dependently modifies the potential energies of the active surface when adsorbed on Co. Therefore, the occupied p-orbital states of Se_c in Co + 1L(**D**) are located near E_F, while those of Co + 1L(**U**) are located far below E_F (the orange downward triangles in Fig. 2a and c). Recalling that the Co + 1L(**U**) can be divided into Co–$InSe_2$ and InSe, while Co + 1L(**D**) consists of Co–InSe and $InSe_2$, Se_c is selectively hybridized with Se_s/Se_i for Co + 1L(**U**)/Co + 1L(**U**). Thus, the filled p-Se_s state in Co + 1L(**U**) is located even further away, while it comes closer to E_F and coincides with that of Se_c in Co + 1L(**D**) (marked by the red downward triangles). Correspondingly, the ε_{pz}-centre/ε_p-centre of Se_s is −3.15/−3.58 eV in Co + 1L(**U**), and the values significantly shift closer to zero (E_F) in Co + 1L(**D**) by having −1.58/−1.97 eV. The values are given for the α-spin state that is located closer to E_F than its β-spin counterpart.

The upward shift of $\varepsilon_{\text{pz-centre}}/\varepsilon_{\text{p-centre}}$ assists the electron transfer from Co to In_2Se_3 in Co + 1L(**D**) and this promotes H* adsorption through the hybridization of the Se_a-p and H-s orbitals (Fig. 2b and d). Eventually, polarization switching turns HER activity "ON" and "OFF", by showing ΔG_{H^*} for Co+1L(**D**) = 0.079 eV < 0.2 eV, while having ΔG_{H^*} for Co+1L(**U**) = 0.49 eV > 0.2 eV. Note that the ΔG_{H^*} values are provided after finding an active site among various Se_s (Fig. S16†). Each Se_s gives a slightly different ΔG_{H^*} due to the difference in the local structures but shows $\Delta G_{H^*} < 0.2$ eV for Co + 1L(**D**) in all cases. Because the Co metal slab directly modulates the activity of the In_2Se_3 based on strong chemical bonding, Co + 1L(**D**) can be categorized as a "direct catalyst".

The "indirect" switchable catalyst: a case with Co + a bilayer of In_2Se_3

The effect of the Co substrate can be further investigated by stacking one more In_2Se_3 on top of Co + 1L, creating Co + 2L. Since Co + 1L(**D**) has been identified as an effective metal in the previous section, it is informative to consider Co + 2L(**D**) as a composite of an active layer 1L(**D**) and an effective metallic substrate Co + 1L(**D**). Fig. 3a illustrates the CDD between the substrate Co + 1L(**D**) and the active material 1L(**D**), where $\Delta\rho_{[\text{Co + 1L}]\text{ + 1L}}$ is obtained using eqn (8) but replacing Co with Co + 1L. Due to the introduction of the Co substrate, the CDD between the two 1L(**D**)s in Co + 2L(**D**) is significantly amplified compared to the case of 2L(**D**) without Co (Fig. S17†). Correspondingly, the physical interlayer distance (d) between the 1L layers was noticeably reduced by 0.5 Å from 3.93 Å to 3.43 Å when introducing Co (Fig. 3a and S17†). Furthermore, the excess charge (the red arrow) is observed at the top of Se_s within the Co + 2L(**D**), and this will act again as a 'glue' for assisting hydrogen attachment (Fig. 3a). On the contrary, the charge deficiency (the blue arrow) shown at the top of Se_s for Co + 2L(**U**) implies that the hydrogen adsorption will be less favoured (Fig. 3c).

Focusing on PDOS, the local VBM-1 p-states of the outer surface atoms in the lower (Se_l) and upper (Se_s) In_2Se_3 layers coincide entirely in terms of electronic energy, as indicated by the blue downward triangles. Due to the charge transfer between Co and the first In_2Se_3, the electron tunnelling channel opens up across the two In_2Se_3 layers. Then, a well-connected electron transport channel near E_F evolves from the substrate to the active layer, efficiently supplying electrons for the HER. Note that the effect of the Co substrate is now weaker than that in the above-mentioned Co + 1L case and the induced metallicity and strain on the active surface are absent.

$\varepsilon_{\text{pz-centre}}/\varepsilon_{\text{p-centre}}$ for Co + 2L(**D**) is −1.28/−1.62 eV and ΔG_{H^*} is obtained as 0.111 eV in the "HER-ON" state. Such channel-opening results from the charge transfer between Co and In_2Se_3, which is not observed in 2L(**D**) (Fig. S17†). The corresponding potential energy profiles are provided in Fig. S18.†

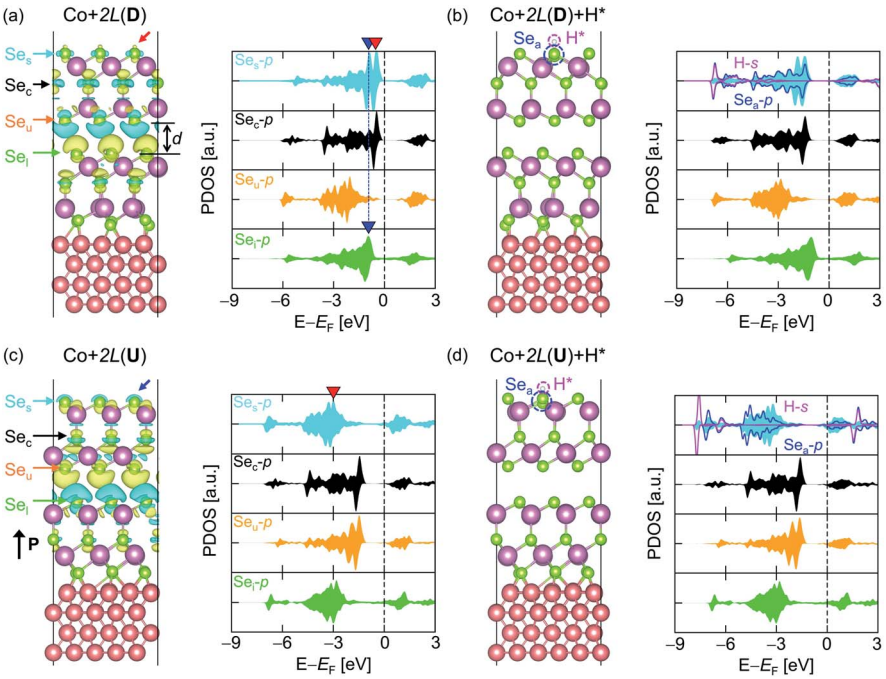

Fig. 3 Atomic models (left) and the PDOS (right) for (a) Co + 2L(**D**), (b) Co + 2L(**D**) + H*, (c) Co + 2L(**U**), and (d) Co + 2L(**U**) + H*. For the models without H*, CDDs between the two In_2Se_3 layers are overlaid with the atomic models. The isovalue is 0.0002 **e**/Å^3, while the yellow and cyan colours represent positive (excessive electrons) and negative (deficient electrons) values, respectively. d = 3.43 Å indicates an interlayer distance between the 1L layers within Co + 2L(**D**). Red/blue arrows indicate the excessive/deficient charge at the active surface of Co + 2L(**D**)/Co + 2L(**U**). The types of atoms in the models are indicated by coloured arrows, and the same colours are used to represent the PDOS: cyan, black, orange, green, blue, and magenta represent Se_s, Se_c, Se_u, Se_l, Se_a, and H*, respectively. In plotting the PDOS, p-orbitals for Se and s-orbitals for H are used. The blue downward triangles indicate the energy location of the local VBM-1 for Se_s and Se_l. The red downward triangle represents the position of the p-band peak for Se_s ($\varepsilon_{\text{p-peak}}$).

When a hydrogen is attached, the electronic state of the upper In_2Se_3 layer (Se_s, Se_c, and Se_u) shifts downward, while that of the lower In_2Se_3 layer (Se_l) remains unchanged (Fig. 3b). With the hydrogen desorption, the tunnelling channel from the Co to the top 1L(**D**) opens up again (Fig. 3a). The electron tunnelling channel in Co + 2L(**U**) is similarly connected from Co + 1L(**U**) to the top 1L(**U**) but the filled p-Se_s states are located far below E_F (Fig. 3c and d). $\varepsilon_{pz\text{-}centre}/\varepsilon_{p\text{-}centre}$ is −3.33/−3.75 eV for Co + 2L(**U**) with $\Delta G_{H^*} = 1.665$ eV in "HER-OFF". Thus, ON/OFF switchable HER is again achieved with Co + 2L. Since the Co metal slab indirectly modulates the activity of the In_2Se_3 based on weak physisorption (the van der Waals interaction between the two In_2Se_3 without induced metallicity and strain) and tunnelling, Co + 2L(**D**) is labelled as an "indirect catalyst".

The descriptors for HER-ON/OFF states

Fig. 4a provides a schematic diagram that summarizes the HER activities of the models introduced throughout this work and Fig. 4b and c visualize the evaluations of the ON/OFF states for HER based on ΔG_{H^*}. Prior to their incorporation in the heterostructure, monolayer In_2Se_3, bilayer In_2Se_3, and the bare metal Co are all inactive materials for HER. Upon stacking monolayer In_2Se_3 on top of Co (Fig. 4b), the ΔG_{H^*} of Co + 1L(**U**) and Co + 1L(**D**) is 0.49 eV (>0.20 eV) and 0.082 eV (<0.20 eV), respectively. This identifies Co + 1L(**U**) as "HER-OFF" and Co + 1L(**D**) as "HER-ON" states. Therefore, the HER activities of 1L stacked on Co can be turned "ON" and "OFF" simply by controlling its polarity to **D** and **U** using external stimuli. Furthermore, the switchable HER activity can be observed even when stacking bilayer In_2Se_3 on the Co slab (Fig. 4c). After adsorbing one more In_2Se_3 layer on top of Co + 1L through van der Waals interactions, Co + 2L(**D**) and Co + 2L(**U**) are also respectively assigned as "HER-ON" and "HER-OFF". The ΔG_{H^*} values of Co + 2L(**D**) and Co + 2L(**U**) are 0.11 eV < 0.20 eV and 1.67 eV > 0.20 eV, respectively.

The origins of ON–OFF switching can be systematically analysed based on Table 1, providing the ΔG_{H^*} and ON/OFF status of the models in Fig. 4 with proper descriptors. First, the effect of ferroelectric switching is indicated by $\varepsilon_{pz\text{-}centre}$ and $\varepsilon_{p\text{-}centre}$. For all of the models, the values are closer to zero (the filled p-Se_s are closer to E_F) in **D** than **U** and modulating the structure from **U** to **D** significantly reduces ΔG_{H^*}. Since **U** and **D** in each model are basically the same material with different ferroelectric states, $\varepsilon_{pz\text{-}centre}$, $\varepsilon_{p\text{-}centre}$, and $\varepsilon_{p\text{-}peak}$ are intuitive descriptors for comparing the HER efficiencies of **U** and **D**. However, $\varepsilon_{pz\text{-}centre}/\varepsilon_{p\text{-}centre}/\varepsilon_{p\text{-}peak}$ cannot be the only parameters for HER efficiency when it comes to the comparison of two distinct materials since the evaluation of HER efficiency basically contains the precise assessment of hydrogen adsorption energies. For example, as the stiffness or stability of In_2Se_3 changes with the thickness, the hydrogen adsorption energy will also change with the number of In_2Se_3 layers. While 2L(**D**) shows a higher εs and smaller ΔG_{H^*} than its 1L(**D**) counterpart, the assessment of thickness-dependent HER activity cannot be discussed simply on the basis of $\varepsilon_{pz\text{-}centre}/\varepsilon_{p\text{-}centre}/\varepsilon_{p\text{-}peak}$ when the In_2Se_3 becomes thicker.

Meanwhile, the Co metal slab significantly modifies the electronic structure of In_2Se_3. Co acts as an electron reservoir and provides an electron transfer channel to activate In_2Se_3. This is particularly enabled by the ferromagnetism of Co because Co-induced spin decomposition on In_2Se_3 attracts α spin to shift closer to E_F as a major charge transfer channel. If In_2Se_3 undergoes the 'strong' Co effect, the nature of In_2Se_3 will be modified through applied strain and slight metallization due to the Co–In_2Se_3 hybridizations. Even if the In_2Se_3 undergoes only a 'weak' Co effect, the electrons will be efficiently supplied to the active surface while the electronic structure of In_2Se_3 remains intact.

Achieving ON and OFF states of HER can be understood as manipulating the synergy of the ferroelectric switching of In_2Se_3

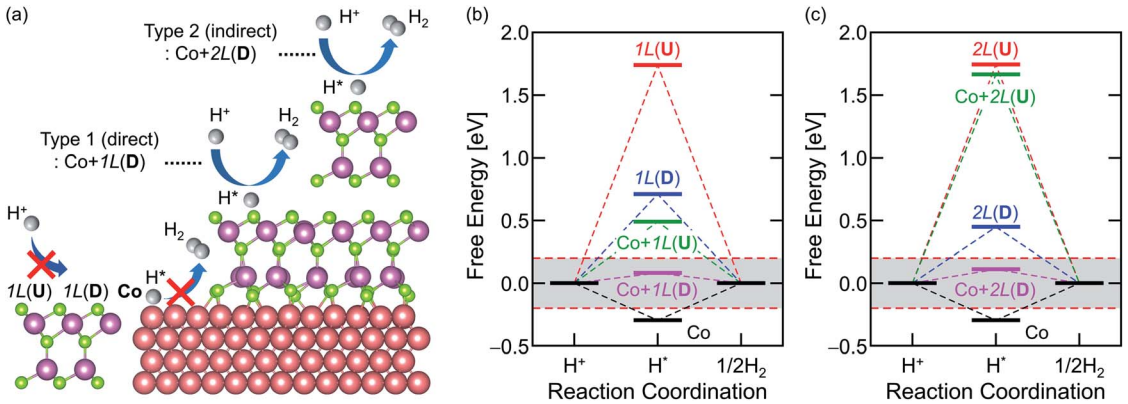

Fig. 4 (a) A schematic diagram of HER based on In_2Se_3 FE-ZB′ and Co. First, neither Co nor 1L is a suitable HER catalyst for opposite reasons: while hydrogens adsorb too strongly on a bare Co metal surface, they are unlikely to adsorb on an isolated In_2Se_3 regardless of the polarity (**U** or **D**). Second, Co metal surfaces that are decorated by **D** state-In_2Se_3 of either 1L or 2L are good HER catalysts. The atomic-level origin for these HER activities is distinct for monolayer and bilayer In_2Se_3, which are identified as "direct" and "indirect", respectively. A free energy diagram for HER at zero potential on various Co–In_2Se_3 heterostructures with (b) 1L and (c) 2L. The red, blue, green, magenta, and black lines indicate 1L/2L(**U**), 1L/2L(**D**), Co + 1L/2L(**U**), Co + 1L/2L(**D**), and bare Co cases, respectively. The grey shaded area indicates the condition where $|\Delta G_{H^*}| <$ 0.20 eV.

Table 1 Calculated ΔG_{H^*} and evaluation of HER ON/OFF states for all the models with different polarizations (P) of D/U considered in this work, together with ε_{p_z}-centre, $\varepsilon_{p\text{-centre}}$, and $\varepsilon_{p\text{-peak}}$ for α/β spin and the effect of the Co slab. For the cases without Co, only the α spin is considered

Model	P	ΔG_{H^*} [eV]	ON/OFF[a]	$\varepsilon_{pz\text{-centre}}$ (α/β) [eV]	$\varepsilon_{p\text{-centre}}$ (α/β) [eV]	$\varepsilon_{p\text{-peak}}$ (α/β) [eV]	Co effect[b]
Co + 1L	**D**	0.082	ON	−1.58/−1.78	−1.97/−2.16	−0.91/−1.14	Strong
	U	0.490	OFF	−3.15/−3.32	−3.58/−3.64	−3.17/−3.27	
Co + 2L	**D**	0.111	ON	−1.28/−1.45	−1.62/−1.79	−0.47/−0.65	Weak
	U	1.665	OFF	−3.33/−3.48	−3.75/−3.91	−3.00/−3.19	
1L	**D**	0.710	OFF	−1.67	−2.03	−0.87	None
	U	1.740		−2.86	−3.26	−2.48	
2L	**D**	0.448		−1.35	−1.71	−0.55	
	U	1.745		−3.23	−3.63	−2.85	

[a] 'ON' if $|\Delta G_{H^*}| < 0.20$ eV, 'OFF' if not. [b] 'Strong' if the active In_2Se_3 is directly attached on Co, 'weak' if the active In_2Se_3 is influenced by but not directly attached to Co, 'None' if there is no Co in the atomic model.

and the ferromagnetic Co effects. In the absence of Co (few-layer In_2Se_3 with no Co effect), ΔG_{H^*} for **D** is always more favourable for HER than its **U** counterpart as can be anticipated in the previous report[12] but always stays "OFF" for all cases. When Co is introduced without metalizing In_2Se_3 or hybridizations (Co + 2L with a 'weak' Co effect), the electrons are transferred to the active surface through tunnelling to promote hydrogen adsorption. ΔG_{H^*} is reduced both in **D** and **U** so that the ON(**D**)–OFF(**U**) states of HER are achieved. Co + 2L(**D**) has been labelled as an 'indirect' catalyst in this paper. For 'strong' Co effects with interfacial strain, induced metallicity, and hybridizations on In_2Se_3 (Co + 1L), ΔG_{H^*} is further reduced by direct charge transfer. Then, ON(**D**)–OFF(**U**) states of HER are again achieved. Having a ΔG_{H^*} of almost zero, Co + 1L(**D**) can be understood as a more efficient catalyst than Co + 2L(**D**) and labelled as a 'direct' catalyst.

Conclusions

In summary, this theoretical work provides a brief concept design and insight into the construction of a dynamic catalyst based on a 2D-FE material-transition metal complex. The main points in this work can be summarized as follows:

• A theoretical design of a 2D material-based heterostructure for a switchable catalyst.

• A theoretical formulation on how the ferroelectric modulation of the 2D material gives rise to an active/inactive HER surface through coupling with a non-noble metal substrate, without introducing chemical modifications.

Owing to the unique quintuple structure and intrinsic ferroelectricity of the III_2VI_3 compound, the stacking of In_2Se_3 onto the ferromagnetic transition metal Co slab enables control over the hydrogen adsorption onto In_2Se_3, thereby switching the HER on and off. The underlying principle is the polarization-dependent control of the electron supply from Co to In_2Se_3, which is based on the synergy of ferroelectric switching of In_2Se_3 and the effect of ferromagnetic metal Co. Correspondingly, the "direct" and "indirect" catalysts are defined in terms of the bonding nature of the electron supply paths from Co to In_2Se_3 (either chemical bonding at Co + 1L In_2Se_3 or tunnelling through physical bonding at Co + 2L In_2Se_3).

For the design of switchable electrocatalysts based on 2D-FE III_2VI_3 heterostructures, this work mainly focuses on the principles of catalytic activities of the heterostructure through theoretical discussions by taking In_2Se_3 as an example III_2VI_3 material. For the viability of ON–OFF conversion, the controllability of the polarization energy barrier of In_2Se_3 in response to external stimuli without (Fig. S19†) and with (Fig. S20 and S21†) the presence of a Co slab was also briefly investigated. The energy barrier for **D**–**U** conversion in a neutral system implies the reasonable stability of the structure. The barrier can be significantly reduced by applying an electric field or net charge. It is important to recall that a switchable non-volatile memory based on the polarization conversion of few-layer In_2Se_3 (~2.6 nm) was realized experimentally by applying a gate bias on top of a metallic gate.[10] Consistent with the experimental achievement, the backgate voltage that gives the net charge on the system can modulate the energy barrier between **D** and **U** even when the In_2Se_3 is adsorbed on the Co substrate (Fig. S20 and S21†). While brief indications of the viability of the ON–OFF conversion are provided, the next step will be to theoretically expand and experimentally realize this brief idea. Thorough theoretical discussions on the thickness-dependent ΔG_{H^*} of ferroelectric In_2Se_3, metal species-dependent HER activity of the metal-In_2Se_3 heterostructure and ON–OFF conversion dynamics within the non-equilibrium external stimuli will be pursued in the following studies. In this effort, the design principle and theoretical analysis provided in this work will offer key guidances for the experimental development of switchable electrocatalysts based on 2D-FE III_2VI_3 heterostructures in the future.

Conflicts of interest

There are no conflicts to declare.

Acknowledgements

All the simulation data in this work were generated and analysed with the active use of the NURION (KISTI-5) high-performance computing resources supported by the Korea Institute of Science and Technology Information (KISTI) (KSC-2019-CRE-0199 & KSC-2020-CRE-0300). This work was carried out under the financial support from the institutional R&D

program of KISTI (K-21-L02-C10) and the National R&D program of the National Research Foundation (NRF) (NRF-2020R1F1A1075573) funded by the Ministry of Science and ICT of Korea. I would like to thank my dear friend Min Jong Noh for all of the support and valuable discussions regarding this research.

Notes and references

1 C. Cui, F. Xue, W. J. Hu and L. J. Li, *npj 2D Mater. Appl.*, 2018, **2**, 18.
2 Z. Guan, H. Hu, X. Shen, P. Xiang, N. Zhong, J. Chu and C. Duan, *Adv. Electron. Mater.*, 2020, **6**, 1–30.
3 W. Xiong, K. Huang and S. Yuan, *J. Mater. Chem. C*, 2019, **7**, 13518–13525.
4 H. Li, S. Hu, S. Zhao and C. Lan, *Chem. Phys. Lett.*, 2020, **749**, 137404.
5 L. Debbichi, O. Eriksson and S. Lebègue, *J. Phys. Chem. Lett.*, 2015, **6**, 3098–3103.
6 W. Ding, J. Zhu, Z. Wang, Y. Gao, D. Xiao, Y. Gu, Z. Zhang and W. Zhu, *Nat. Commun.*, 2017, **8**, 14956.
7 Y. Zhou, D. Wu, Y. Zhu, Y. Cho, Q. He, X. Yang, K. Herrera, Z. Chu, Y. Han, M. C. Downer, H. Peng and K. Lai, *Nano Lett.*, 2017, **17**, 5508–5513.
8 S. Li, J. Z. Liu, M. T. Edmonds, L. Yu, J. L. Collins, Y. Lou, C. Xu, C. Zheng, Z. Wei, M. S. Fuhrer, D. Kim, J. Seidel, Y. Zhang, W.-X. Tang, Y. Zhu, M. Li and L. Zhu, *Sci. Adv.*, 2018, **4**, eaar7720.
9 C. Cui, W. Hu, X. Yan, C. Addiego, W. Gao, Y. Wang, Z. Wang, L. Li, Y. Cheng, P. Li, X. Zhang, H. N. Alshareef, T. Wu, W. Zhu, X. Pan and L.-J. Li, *Nano Lett.*, 2018, **18**, 1253–1258.
10 S. Wan, Y. Li, W. Li, X. Mao, C. Wang, C. Chen, J. Dong, A. Nie, J. Xiang, Z. Liu, W. Zhu and H. Zeng, *Adv. Funct. Mater.*, 2019, **29**, 1808606.
11 P. Hou, S. Xing, X. Liu, C. Chen, X. Zhong, J. Wang and X. Ouyang, *RSC Adv.*, 2019, **9**, 30565–30569.
12 X. Tang, J. Shang, Y. Gu, A. Du and L. Kou, *J. Mater. Chem. A*, 2020, **8**, 7331–7338.
13 H. Shi, M. Li, A. Shaygan Nia, M. Wang, S. Park, Z. Zhang, M. R. Lohe, S. Yang and X. Feng, *Adv. Mater.*, 2020, **32**, 1907244.
14 C. F. Fu, J. Sun, Q. Luo, X. Li, W. Hu and J. Yang, *Nano Lett.*, 2018, **18**, 6312–6317.
15 P. Zhao, Y. Ma, X. Lv, M. Li, B. Huang and Y. Dai, *Nano Energy*, 2018, **51**, 533–538.
16 A. Kakekhani, S. Ismail-Beigi and E. I. Altman, *Surf. Sci.*, 2016, **650**, 302–316.
17 Y. Zhang, M. Xie, V. Adamaki, H. Khanbareh and C. R. Bowen, *Chem. Soc. Rev.*, 2017, **46**, 7757–7786.
18 L. Cui, Y. Xu, L. Niu, W. Yang and J. Liu, *Nano Res.*, 2017, **10**, 595–604.
19 F. Erogbogbo, T. Lin, P. M. Tucciarone, K. M. Lajoie, L. Lai, G. D. Patki, P. N. Prasad and M. T. Swihart, *Nano Lett.*, 2013, **13**, 451–456.
20 S. Hao, L. Yang, L. Cui, W. Lu, Y. Yang, X. Sun and A. M. Asiri, *Nanotechnology*, 2016, **27**, 46.
21 Y. Sofue, K. Nomura and A. Inagaki, *Chem. Commun.*, 2020, **56**, 4519–4522.
22 Y. Ma, M. Li, K. Shi, Z. Chen, B. Yang, D. Rao, X. Li, W. Ma, S. Hou, G. Gou and H. Yao, *New J. Chem.*, 2020, **44**, 16045–16053.
23 P. Sabatier, *Ber. Dtsch. Chem. Ges.*, 1911, **44**, 1984–2001.
24 J. K. Nørskov, T. Bligaard, A. Logadottir, J. R. Kitchin, J. G. Chen, S. Pandelov and U. Stimming, *J. Electrochem. Soc.*, 2005, **152**, J23–J26.
25 D. Deng, K. S. Novoselov, Q. Fu, N. Zheng, Z. Tian and X. Bao, *Nat. Nanotechnol.*, 2016, **11**, 218–230.
26 C. Wang, J. Huang, J. Chen, Z. Xi and X. Deng, *Front. Chem.*, 2019, **7**, 131.
27 X. Long, W. Qiu, Z. Wang, Y. Wang and S. Yang, *Mater. Today Chem.*, 2019, **11**, 16–28.
28 P. Raybaud, J. Hafner, G. Kresse, S. Kasztelan and H. Toulhoat, *J. Catal.*, 2000, **189**, 129–146.
29 B. Hinnemann, P. G. Moses, J. Bonde, K. P. Jørgensen, J. H. Nielsen, S. Horch, I. Chorkendorff and J. K. Nørskov, *J. Am. Chem. Soc.*, 2005, **127**, 5308–5309.
30 H. Wang, Z. Lu, S. Xu, D. Kong, J. J. Cha, G. Zheng, P. C. Hsu, K. Yan, D. Bradshaw, F. B. Prinz and Y. Cui, *Proc. Natl. Acad. Sci. U. S. A.*, 2013, **110**, 19701–19706.
31 M. A. Lukowski, A. S. Daniel, F. Meng, A. Forticaux, L. Li and S. Jin, *J. Am. Chem. Soc.*, 2013, **135**, 10274–10277.
32 X. Huang, Z. Zeng and H. Zhang, *Chem. Soc. Rev.*, 2013, **42**, 1934–1946.
33 Q. Tang and D. E. Jiang, *ACS Catal.*, 2016, **6**, 4953–4961.
34 J. Zhu, Z. C. Wang, H. Dai, Q. Wang, R. Yang, H. Yu, M. Liao, J. Zhang, W. Chen, Z. Wei, N. Li, L. Du, D. Shi, W. Wang, L. Zhang, Y. Jiang and G. Zhang, *Nat. Commun.*, 2019, **10**, 1348.
35 G. Zhao, K. Rui, S. X. Dou and W. Sun, *Adv. Funct. Mater.*, 2018, **28**, 1803291.
36 J. J. Mortensen, L. B. Hansen and K. W. Jacobsen, *Phys. Rev. B: Condens. Matter Mater. Phys.*, 2005, **71**, 035109.
37 B. Hammer, L. B. Hansen and J. K. Nørskov, *Phys. Rev. B: Condens. Matter Mater. Phys.*, 1999, **59**, 7413–7421.
38 E. L. Briggs, D. J. Sullivan and J. Bernholc, *Phys. Rev. B: Condens. Matter Mater. Phys.*, 1995, **52**, R5471–R5474.
39 G. Kresse and J. Furthmüller, *Phys. Rev. B: Condens. Matter Mater. Phys.*, 1996, **54**, 11169–11186.
40 N. M. Marković, B. N. Grgur and P. N. Ross, *J. Phys. Chem. B*, 1997, **101**, 5405–5413.
41 A. Hjorth Larsen, J. Jørgen Mortensen, J. Blomqvist, I. E. Castelli, R. Christensen, M. Dułak, J. Friis, M. N. Groves, B. Hammer, C. Hargus, E. D. Hermes, P. C. Jennings, P. Bjerre Jensen, J. Kermode, J. R. Kitchin, E. Leonhard Kolsbjerg, J. Kubal, K. Kaasbjerg, S. Lysgaard, J. Bergmann Maronsson, T. Maxson, T. Olsen, L. Pastewka, A. Peterson, C. Rostgaard, J. Schiøtz, O. Schütt, M. Strange, K. S. Thygesen, T. Vegge, L. Vilhelmsen, M. Walter, Z. Zeng and K. W. Jacobsen, *J. Phys.: Condens. Matter*, 2017, **29**, 273002.
42 R. P. Stoffel, C. Wessel, M.-W. Lumey and R. Dronskowski, *Angew. Chem., Int. Ed.*, 2010, **49**, 5242–5266.
43 A. Togo and I. Tanaka, *Scr. Mater.*, 2015, **108**, 1–5.

44 Y. A. Zhu, D. Chen, X. G. Zhou and W. K. Yuan, *Catal. Today*, 2009, **148**, 260–267.
45 J. Deng, P. Ren, D. Deng and X. Bao, *Angew. Chem., Int. Ed.*, 2015, **54**, 2100–2104.
46 Y. Jiao, Y. Zheng, K. Davey and S. Z. Qiao, *Nat. Energy*, 2016, **1**, 16130.
47 H. Shu, D. Zhou, F. Li, D. Cao and X. Chen, *ACS Appl. Mater. Interfaces*, 2017, **9**, 42688–42698.
48 Y. Zhang, X. Chen, Y. Huang, C. Zhang, F. Li and H. Shu, *J. Phys. Chem. C*, 2017, **121**, 1530–1536.
49 Y. Cui, M. Li, X. Zhang, S. Wang and Y. Huang, *Green Energy Environ.*, DOI: 10.1016/j.gee.2021.01.002.
50 B. Hammer and J. K. Norskov, *Nature*, 1995, **376**, 238–240.
51 J. K. Nørskov, F. Abild-Pedersen, F. Studt and T. Bligaard, *Proc. Natl. Acad. Sci. U.S.A.*, 2011, **108**, 937–943.
52 C. Jin, X. Tang, X. Tan, S. C. Smith, Y. Dai and L. Kou, *J. Mater. Chem. A*, 2019, **7**, 1099–1106.
53 Y. Jiao, Y. Zheng, M. Jaroniec and S. Z. Qiao, *Chem. Soc. Rev.*, 2015, **44**, 2060–2086.
54 Z. W. Chen, L. X. Chen, Z. Wen and Q. Jiang, *Phys. Chem. Chem. Phys.*, 2019, **21**, 23782–23802.
55 Z. Su, R. Pang, X. Ren and S. Li, *J. Mater. Chem. A*, 2020, **8**, 17238–17247.
56 L. Zhang, W. Qin, L. Li, S. Li, P. Cui, Y. Jia and Z. Zhang, *Nanoscale*, 2018, **10**, 18988–18994.

